PHYSICAL REVIEW E **91**, 032410 (2015)

Crystal-liquid interfacial free energy of hard spheres via a thermodynamic integration scheme

Ronald Benjamin[*] and Jürgen Horbach[†]

Institut für Theoretische Physik II: Soft Matter, Heinrich Heine-Universität Düsseldorf, Universitätsstraße 1, 40225 Düsseldorf, Germany

(Received 3 December 2014; revised manuscript received 24 February 2015; published 16 March 2015)

The hard-sphere crystal-liquid interfacial free energy γ_{cl} is determined from molecular dynamics simulations using a thermodynamic integration (TI) scheme. The advantage of this TI scheme compared to previous methods is to successfully circumvent hysteresis effects due to the movement of the crystal-liquid interface. This is accomplished by the use of extremely-short-range and impenetrable Gaussian flat walls that prevent the drift of the interface while imposing a negligible free-energy penalty. We find that it is crucial to analyze finite-size effects in order to obtain reliable estimates of γ_{cl} in the thermodynamic limit.

DOI: 10.1103/PhysRevE.91.032410 PACS number(s): 68.08.−p, 05.70.Np, 64.70.D−, 82.20.Wt

I. INTRODUCTION

Since the discovery of a fluid-to-solid transition in hard spheres by computer simulations [1], the hard-sphere model has become one of the paradigms [2] for the study of nucleation and crystal growth [3–7]. The simplicity of the hard-sphere interaction potential is well suited for the development of theoretical and computational approaches that allow for quantitative predictions in the context of crystallization phenomena [8–15]. The crucial thermodynamic parameter that governs the mechanism of homogeneous nucleation and subsequent growth of the crystal from the melt is the crystal-liquid interfacial free energy γ_{cl}, defined as the reversible work required to form a unit area of a crystal-liquid interface [16]. The homogeneous nucleation rate and the final morphology of the resulting crystal are strongly dependent on the magnitude and anisotropy of this quantity [17–21].

Several simulation and theoretical approaches (based on density-functional theory) have been attempted to determine the interfacial free energy of hard-sphere systems, though there have been some discrepancies in the results obtained from these various methods [22–29]. A direct determination of γ_{cl} for hard-sphere systems was made in Ref. [22] using a thermodynamic integration [30,31] approach known as the cleaving-wall method. Later, the estimates for γ_{cl} were revised [27] after fixing an error in the previous thermodynamic integration (TI) scheme. The same authors carried out TI simulations with the soft-sphere potential and extrapolated the results to the hard-sphere limit [24,25]. Data in Ref. [24] were a little higher than those reported for the pure hard-sphere system [27]. Recent estimates from an indirect approach based on capillary fluctuations [28] as well as from the tethered Monte Carlo approach [29] were about 10% higher than those reported in Ref. [27].

In the cleaving-wall scheme [22,27], thermodynamic integration is carried out by using an external wall, consisting of particles arranged in an ideal lattice structure, to split the bulk phases and then join them together. Finally, the walls are removed, resulting in crystal and liquid phases separated by two interfaces. In this approach, there are uncontrolled hysteresis errors in the last step when the external walls are removed. When both phases are joined together, the interface is formed at the walls. However, when such cleaving walls are gradually removed, the interface drifts on account of thermal fluctuations. In long simulations, the interfaces can travel far from the walls by freezing at one end and simultaneously melting at the other end [27,32,33]. As a result, the reverse process (when the cleaving walls are reinserted) does not retrace the same path as the forward process, showing the existence of hysteresis. This affects the accuracy in the final estimates of γ_{cl}. While the interfacial drift is not a problem for liquid-liquid interfaces [34], it is far more severe for the crystal-liquid interface and needs to be overcome in order to obtain accurate values for γ_{cl}.

In a recent work, we have developed a TI scheme to compute γ_{cl} for the Lennard-Jones potential [35]. Our method is able to circumvent problems associated with the drift of the crystal-liquid interface and provides a better control of hysteresis errors associated with the latter drift. The strategy is to use extremely-short-range and flat Gaussian walls to constrain the position of the interface while imposing a negligible free-energy penalty. Another difference of our scheme is the use of structured walls consisting of frozen-in crystalline layers to smoothly transform the system from separate bulk phases to two interfaces in contact with the bulk fluid and crystal phases.

Apart from the TI scheme, the reliability of γ_{cl} estimates also depends on properly accounting for finite-size effects. However, few previous works on the determination of γ_{cl} via molecular simulations include a discussion on finite-size effects. In a recent work, Schmitz *et al.* [34] proposed a scaling relation based on capillary-wave theory, to take into account finite-size corrections and get accurate values for the interfacial free energies in the thermodynamic limit. In our earlier work [35] on the crystal-liquid interfacial free energy for Lennard-Jones systems, results consistent with their theory were obtained.

In this work, we compute γ_{cl} for hard spheres using molecular dynamics (MD) in combination with TI. We will determine γ_{cl} for the (100), (110), and (111) orientations of the face-centered-cubic crystal-liquid interface. The hard-sphere interactions are described by a very-short-range inverse power-law potential (see below). The reason for using such a short-range continuous potential is the easy adaptability of our TI scheme developed for the continuous Lennard-Jones potential into the soft-sphere potential. Since our TI scheme involves a direct modification of the interaction potential, it is easier

---

[*] rbenjamin.phys@gmail.com

[†] horbach@thphy.uni-duesseldorf.de

1539-3755/2015/91(3)/032410(10)

to fit it into a conventional time-driven MD simulation for continuous potentials rather than into a collisional event-driven MD algorithm for a discontinuous hard-sphere potential [36].

To account for errors due to finite-size effects and estimate γ_{cl} in the thermodynamic limit, a careful analysis was carried out at several system sizes in the framework of capillary-wave theory [34,37]. We obtain results consistent with the predictions of capillary-wave theory showing that the introduction of the flat wall does not suppress capillary fluctuations. The success of our scheme indicates that our TI approach is also well suited for very-short-range potentials.

In the next section, we introduce the potential and then describe the TI scheme in Sec. III. The details of the simulation are given in Sec. IV and results are presented in Sec. V. Finally, we end with a conclusion in Sec. VI.

II. INTERACTION POTENTIAL

Hard-sphere interactions between a particle i at position $\vec{r}_i$ and a particle j at position $\vec{r}_j$, separated by a distance $r_{ij} = |\vec{r}_i - \vec{r}_j|$, are approximated by the inverse power-law potential

$$\phi(r_{ij}) = \epsilon \left(\frac{\sigma}{r_{ij}}\right)^n, \tag{1}$$

with $n = 256$, where ϵ and σ set the energy and length scale, respectively. For computational efficiency, the potential was cut off at a distance $r_{\mathrm{c}} = 1.2\sigma$, where the potential has a value of $10^{-21}\epsilon/k_{\mathrm{B}}T$. With the exponent $n = 256$, the parameters for solid-fluid coexistence at the temperature $k_{\mathrm{B}}T = 1.0\epsilon$ (with k_{B} the Boltzmann constant) are very close to those for the hard-sphere system [6], in agreement with recent findings [38] (see below).

III. METHOD

A. The TI scheme

The interfacial free energy γ_{cl} is the excess free-energy per area that results from the formation of an interface between the crystal and the liquid phase. It can be expressed via the difference between the free energy of the inhomogeneous system with crystal-liquid interface F_{cl} and the sum of the bulk free energies of the crystal and liquid F_{c} and F_{l}, respectively,

$$\gamma_{\mathrm{cl}} = \frac{F_{\mathrm{cl}} - (F_{\mathrm{c}} + F_{\mathrm{l}})}{A}, \tag{2}$$

with A the area of the interface.

Computing γ_{cl} via thermodynamic integration involves joining together bulk crystal and liquid phases at coexistence to form an inhomogeneous system involving the individual phases separated by two interfaces. To ensure a path with minimal hysteresis, the crystal phase should be perturbed as little as possible such that no stress is generated in the crystal when it comes into contact with the liquid phase.

Here we provide a TI scheme to compute γ_{cl} for the inverse power potential (1). Our TI scheme is based on an earlier approach used to obtain the crystal-liquid interfacial free energy for a Lennard-Jones potential [35]. Initially, bulk liquid and crystal phases are simulated in a box with dimensions $L_{\mathrm{x}} \times L_{\mathrm{y}} \times L_{\mathrm{z}}$ such that the two phases have the same volume but different particle numbers. The final state comprises two crystal-liquid interfaces connecting the bulk phases, with a total length $2L_{\mathrm{z}}$ along the z direction. Our scheme consists of the six following steps to create a crystal-liquid interface.

Step 1. The initial thermodynamic state of our system consists of separate bulk liquid and crystal phases with periodic boundary conditions in all directions, while the final state involves the liquid and crystal phases separated by two interfaces. To reach the final state, at some point during the transformation, interactions between the two sides of each phase through the periodic boundaries must be switched off, while the interactions between the two phases must be turned on. While rearranging the periodic boundaries, it must be ensured that the particles belonging to each phase remain inside their respective simulation cells and do not cross the boundaries such that density of each phase in its box remains at the respective coexistence density. For this purpose, in the first step, a Gaussian flat wall is gradually introduced at both ends of the liquid simulation cell, along the z direction (sketch 1 in Fig. 1). To tackle the short-range forces due to the flat walls, a multiple-time-step algorithm (a shorter time step for the short-range forces due to the walls and a longer time step for forces between the particles) [31] is implemented for computational efficiency.

The other important purpose of introducing such a flat wall is to prevent the drift of the crystal-liquid interface at

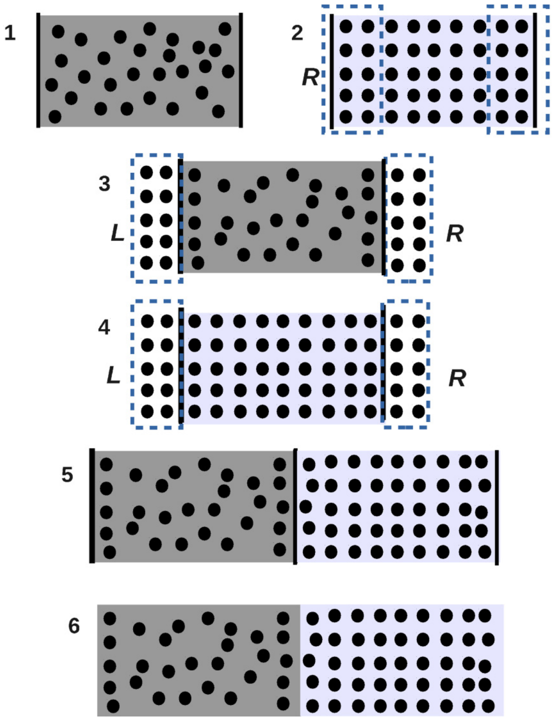

FIG. 1. (Color online) Schematic of the TI scheme adopted in this work. Particles in the light and dark simulation boxes represent the crystal and the liquid phases, respectively. This schematic is a two-dimensional representation of the system. For more details see the text. Here L and R denote the structured walls constructed from the right and left boundaries of the crystal phase in step 2 and attached to the left and right boundaries of the simulation cells in steps 3 and 4, respectively. The schematic for the various steps corresponds to the final state of the system reached at the end of each step.

a later step of the scheme and achieve control over errors due to hysteresis in the TI path. The efficiency of earlier TI schemes [22,24,25,27,33,39] was limited by uncontrolled hysteresis errors arising out of such movement of the crystal-liquid interface on account of thermal fluctuations.

Step 2. Transform a bulk crystal phase at coexistence into one in contact with identical flat walls as in step 1. Similar to the liquid, insertion of the walls requires negligible free energy. However, these walls stop the particles from crossing the boundaries.

Step 3. In addition to the flat walls, a set of solid structured walls is inserted at both ends of the liquid phase. The structured walls are constructed from the positions of particles comprising one to two layers of the crystal phase near the boundaries of the simulation cell and in contact with the flat walls, i.e., particles frozen into a configuration identical to that adopted in an equilibrium simulation of a crystal in contact with a flat wall at the end of step 2, are attached to the two ends of the liquid phase. This is done such that the structured wall constructed from positions of the crystalline layers in contact with the right (left) flat wall at the end of step 2 is attached to the outer left (right) side of the liquid phase (see the sketch in Fig. 1 with the left and right structured walls labeled L and R, respectively). While the x and y coordinates of the left and right structured walls are the same as the crystalline layers in contact with the right and left sides of the crystalline phase, the z coordinates are shifted by $-L_z$ and L_z, respectively.

During this step, the flat walls are still present to prevent particles from crossing the boundaries. During the transformation, the structured walls are gradually switched on, while interactions through the periodic boundaries along the z direction are gradually switched off. Periodic boundary conditions along the x and y directions are kept intact.

Interactions between the particles in the bulk phases and the structured wall are of the same kind as that between the bulk particles. The purpose of this step is to create ordering in the liquid to be compatible with the actual crystal structure such that when the liquid and crystal phases are joined together, there is minimal perturbation and stress in the crystal.

Step 4. Identical structured walls are inserted at either end of the crystal phase obtained from the transformation at step 2. In the presence of the flat walls, interactions between the structured wall and the crystalline phase are turned on while the periodic boundary conditions along the z direction are switched off but kept intact along the x and y directions.

Step 5. In this step, the individual liquid and crystal phases as obtained at the end of steps 3 and 4, respectively, are brought together. This is accomplished by gradually switching on interactions between the two phases while simultaneously switching off the interaction of each phase with the respective structured wall. At the beginning of this step, the simulation cells of the liquid and crystal phases in simultaneous contact with the flat and structured walls at the end of steps 3 and 4, respectively, are placed in contact with each other at one end, along the z direction. Note that both phases interact only with their respective solid walls and not with the wall in contact with the other phase.

At the end of step 5, the resulting thermodynamic state consists of bulk crystal and liquid phases separated by two interfaces whose position is tied to the position of the flat walls with no uncontrolled hysteresis errors during the transformation.

Step 6. The last step involves removing the flat walls and it is difficult to achieve total control over the reversibility of the scheme. Due to thermal fluctuations, the two interfaces can move by melting on one side and refreezing on the other side if the potential barrier due to the walls is weak enough. However, this makes the transformation irreversible since if the walls are reinserted, the position of the interfaces will not coincide with the position of the walls. As a result, in the two simulation boxes a mixture of liquid and crystal phases will be obtained and one cannot retrace the previous steps in the reverse direction to reach the initial state consisting of independent liquid and crystal phases at their respective coexistence densities.

However, due to the short-range flat walls (the shorter the range, the fewer particles interacting with the wall and the smaller the contribution is to the free-energy difference), the contribution of this step to the total free-energy difference is negligible and so is any residual hysteresis. One can choose a flat wall as short ranged as possible to reduce the contribution of this step to be even smaller than the combined statistical errors of the previous steps.

In this work, essentially the above scheme is followed, with slight modifications, since the inverse power potential (1) itself is a short-range potential. Unlike the previous TI scheme [35], where an extremely-short-range flat wall is introduced at the beginning of the scheme, here, in the first step we introduce a flat wall with a range similar to that for the interaction potential between the particles. Only in the final step, the range of this wall is gradually reduced to a value much smaller than the effective size of the particles σ (about 10^4 times less). This trick saves computational time since a very small time step needs to be used only in the final step to integrate the short-range forces. The use of a multiple-time-step algorithm [31] in the final step further improves the computational efficiency of the scheme.

The TI scheme proceeds via the six steps specified above and in each step the transformations are carried out by directly modifying the interaction potential by a parameter λ. This idea is similar to the TI scheme presented in earlier works to compute $\gamma_{\rm cl}$ and the interfacial free energies of liquid and crystal phases in contact with flat and structured walls [35,40,41]. The specific choices of the λ parametrizations adopted below yield smooth thermodynamic integrands, allowing for an accurate numerical calculation of the integrals. Due to the short-range nature of the inverse power potential, the specific parametrizations are model specific and differed from our previous work adopted for the relatively-long-range Lennard-Jones potential.

B. Implementation of the method

In the following, we specify, in detail, the parametrizations adopted for the various steps.

Steps 1 and 2. In the first and second steps, a flat wall is introduced at the ends of both the liquid and crystal simulation cells. The transformation is carried out by gradually increasing the height of the potential barrier. The interaction of a particle

i with the flat wall is modeled by a Gaussian potential

$$u_{\mathrm{fw}}(z_{iw}) = a \exp\left[-\left(\frac{z_{iw}}{b}\right)^2\right], \tag{3}$$

with z_{iw} the distance of the particle from the wall in the z direction. The height and range of the Gaussian potential is determined by the variables a and b, respectively. We choose the temperature $T = 1.0$ and $a = 25k_{\mathrm{B}}T/\epsilon$. With these parameters, the wall is impermeable for the particles. The variable b is set to 0.027σ. For this value of b, the bulk density does not change in the presence of the wall.

The parameter λ is coupled to the flat wall as

$$u_{\mathrm{fw}}(\lambda,z_{iw}) = \lambda^2 u_{\mathrm{fw}}(z_{iw}). \tag{4}$$

At $\lambda = 0$, there is no wall and as λ increases the wall becomes more and more impenetrable.

The λ-dependent Hamiltonian for steps 1 and 2 takes the form

$$H_{1\,(2)}(\lambda) = \sum_{i=1}^{N} \frac{\mathbf{p}_i^2}{2m} + U_{\mathrm{pp}}^{\mathrm{l\,(c)}} + \lambda^2 U_{\mathrm{fw}}^{\mathrm{l\,(c)}}, \tag{5}$$

where $H_{1\,(2)}$ represents the Hamiltonian for the interaction of the flat wall with the liquid (crystal) and $\mathbf{p}_i$ and m denote, respectively, the momentum and mass of particle i, with all particles having the same mass. The potential energy due to particle-particle interactions is represented by $U_{\mathrm{pp}}^{\mathrm{l\,(c)}} = \sum_{i=1}^{N^{\mathrm{l\,(c)}}} \sum_{j=i+1}^{N^{\mathrm{l\,(c)}}} u(r_{ij})$. The interaction potential of particles with the flat wall is denoted by $U_{\mathrm{fw}}^{\mathrm{l\,(c)}} = \sum_{i=1}^{N^{\mathrm{l\,(c)}}} u_{\mathrm{fw}}(z_{iw})$, where the superscript l (c) refers to particles in the liquid (crystal) phase and $N^{\mathrm{l\,(c)}}$ is the total number of liquid (crystal) particles.

Steps 3 and 4. As specified above, two structured walls are constructed by freezing particles into positions adopted by the crystalline particles in contact with the flat walls, at the end of step 2. These walls contain one to two crystalline layers and, as shown in Fig. 1, are juxtaposed at the appropriate ends of the liquid and crystal simulation cells corresponding to steps 3 and 4, respectively. The flat walls are still present to prevent particles from crossing the boundaries. During the transformation, the structured walls are gradually switched on, while interactions through the periodic boundaries along the z direction are gradually switched off.

The λ-dependent Hamiltonian for step 3 is given by

$$H_3(\lambda) = \sum_{\mathrm{i=1}}^{N} \frac{\mathbf{p}_i^2}{2m} + U_{\mathrm{pp}}^{\mathrm{l}} + (1-\lambda)^{256} U_{\mathrm{pp}}^{*\mathrm{l}} + \lambda^{256} U_{\mathrm{pw}}^{\mathrm{l}} + U_{\mathrm{fw}}^{\mathrm{l}}. \tag{6}$$

In Eq. (6) and later on, $U_{\mathrm{pp}}^{*\mathrm{c\,(l)}}$ specifies the periodic boundary interactions, while $U_{\mathrm{pp}}^{\mathrm{c\,(l)}}$ corresponds to the bulk interactions. Interactions between the individual phases and the structured wall particles are described by U_{pw}, where $U_{\mathrm{pw}}^{\mathrm{c\,(l)}} = \sum_{i=1}^{N^{\mathrm{c\,(l)}}} \sum_{j=1}^{N^{\mathrm{w}}} u_{\mathrm{pw}}(r_{ij})$, with N^{w} being the total number of particles in the structured walls. The same inverse power potential is used for u_{pw}, as given by Eq. (1), with the parameter ϵ replaced by ϵ_{pw}. Throughout the transformation in steps 3 and 4 as well as in subsequent steps, $\epsilon_{\mathrm{pw}}/\epsilon = 1$ is kept constant, where ϵ refers to the interaction strength between the particles of the system.

Since the inverse-power potential (1) is very short ranged and the liquid particles present are close to the boundaries of the simulation box at the beginning of this step, a λ parametrization for the periodic boundaries corresponding to a rapidly decaying function with λ ensures a smoothly varying thermodynamic integrand. Effectively, this transformation is carried out by gradually modifying the size of the particles, i.e., $\epsilon[(1-\lambda)\sigma/r]^{256}$ and $\epsilon(\lambda\sigma/r)^{256}$ for switching off the periodic boundaries and switching on the structured walls, respectively.

In the cleaving-wall TI scheme, the interaction between the individual phases and the walls is brought about by moving the walls towards the bulk liquid and crystal phases. This requires the use of a corrugated cleaving plane [27,33], which is compatible with the structure of the wall. In our TI scheme, the interaction between the two phases or between each individual phase and the structured walls takes place across a flat plane. As shown above, this is achieved by directly modifying the interaction potentials to carry out the transformations.

The corresponding Hamiltonian for step 4 is given by

$$H_4(\lambda) = \sum_{\mathrm{i=1}}^{N} \frac{\mathbf{p}_i^2}{2m} + U_{\mathrm{pp}}^{\mathrm{c}} + (1-\lambda)^{8} U_{\mathrm{pp}}^{*\mathrm{c}} + \lambda^{256} U_{\mathrm{pw}}^{\mathrm{c}} + U_{\mathrm{fw}}^{\mathrm{c}}. \tag{7}$$

Since it is necessary to maintain the crystalline structure throughout the transformation, in Eq. (7), the periodic boundaries are switched off gradually (see the power of 8 in front of $U_{\mathrm{pp}}^{*\mathrm{c}}$) such that these interactions become weaker only when the structured walls are already strongly interacting with the crystal phase.

Step 5. In this step, the individual liquid and crystal phases are gradually brought together in the presence of the Gaussian flat walls, while the structured walls are gradually removed. Since the periodic boundary conditions in the two phases are already switched off, only interactions between the two phases need to be turned on (see 5 in Fig. 1). At the end of this step, an inhomogeneous system with crystal and liquid phases separated by two interfaces is created. The positions of the crystal-liquid interfaces are tied to the position of the flat walls and do not drift.

The Hamiltonian corresponding to step 5 is

$$H_5(\lambda) = \sum_{\mathrm{i=1}}^{N_p} \frac{\mathbf{p}_{\mathrm{i}}^2}{2m_i} + U_{\mathrm{pp}}^{\mathrm{c\,(l)}} + \lambda^2 \left(\frac{1+\lambda}{2}\right)^{256} U_{\mathrm{pp}}^{\mathrm{c+l}} + (1-\lambda)^2 (1-\lambda/2)^{256} U_{\mathrm{pw}}^{\mathrm{c\,(l)}} + U_{\mathrm{fw}}^{\mathrm{c\,(l)}}, \tag{8}$$

where the interaction potential between the liquid and crystal phases is denoted by $U_{\mathrm{pp}}^{c+l} = \sum_{i=1}^{N^{\mathrm{l}}} \sum_{j=1}^{N^{\mathrm{c}}} u(r_{ij})$. In Eq. (8), there is a one-to-one correspondence in the λ parametrizations such that interactions between the crystal and liquid phases are turned on while interactions with the structured wall are switched off to ensure a smoothly varying thermodynamic integrand.

Step 6. In the last step, the flat walls are removed such that the final state consists of liquid and crystal phases separated by two interfaces. However, since the range of the flat walls is not insignificant, the contribution of this step cannot be ignored.

Simply switching off the wall in a single step would lead to hysteresis errors. However, by a clever scheme one can reduce the error due to the resulting hysteresis in the TI path to a negligible value such that it does not affect the accuracy in the final estimates of $\gamma_{\rm cl}$. This is achieved by breaking step 6 into two substeps 6a and 6b. In the first substep, the range of the Gaussian flat wall is gradually reduced while maintaining the same height for the potential barrier. In principle, this substep is reversible since the particles still cannot cross the flat-wall barrier at the end of this step. In the next step 6b, the height of the barrier is slowly switched off such that in the end one has the desired state consisting of liquid and crystalline phases separated by two interfaces. This transformation is no longer reversible due to the movement of the interface. However, if the range of the Gaussian flat wall has been reduced significantly in step 6a such that very few particles interact with the wall, the contribution of step 6b would be negligible in comparison to the magnitude of $\gamma_{\rm cl}$ and can be ignored.

The Hamiltonian corresponding to substep 6a is given by

$$H_{\rm 6a}(\lambda) = \sum_{i=1}^{N} \frac{\mathbf{p}_i^2}{2m} + U_{\rm pp}^{1(c)} + U_{\rm fw}^{1(c)}(\lambda), \tag{9}$$

with

$$u_{\rm fw}(z_{iw},\lambda) = a \exp\{-[z_{iw}/b(\lambda)]^2\}, \tag{10}$$

where $U_{\rm fw}^{1(c)}(\lambda) = \sum_{i=1}^{N_{1(c)}} u_{\rm fw}(z_{iw},\lambda)$. In Eq. (10), $b(\lambda) = (1-\lambda)^2 b'$ with $b' = 0.027\sigma$ and λ varies from 0 to 0.893 such that the parameter $b(\lambda)$ is reduced from 0.027σ to 0.0003σ.

In the next substep 6b, the extremely-short-range Gaussian walls are gradually switched off. The Hamiltonian for this substep is

$$H_{\rm 6b}(\lambda) = \sum_{i=1}^{N} \frac{\mathbf{p}_i^2}{2m} + U_{\rm pp}^{1(c)} + (1-\lambda)^2 U_{\rm fw}^{1(c)}. \tag{11}$$

In this last step, b was kept at the same value as at the end of step 6a, viz., $b = 0.0003\sigma$. In principle, the flat wall could be made even more short ranged by varying λ in step 6a up to, say, 0.99. However, our simulations showed that reducing the range of the flat wall to such a low value is unnecessary for our purpose since the combined numerical and statistical errors from 1–5 would be much larger than the total contribution from step 6b.

Generally, the contribution of step 6b depends on the average density of particles in the interface region. Prior work on the crystal-liquid interface corresponding to hard-sphere systems has shown that the density near the interface is the mean of the bulk liquid and solid coexistence densities [32]. Even accounting for capillary fluctuations, the average density will not be very far from this mean value. Therefore, the contribution of step 6b will be close to that obtained for the flat wall–liquid interface. For example, at $b = 0.0003\sigma$, the excess free energy of the fluid in contact with the flat wall was about 10 times less than the statistical errors from steps 1–6a. For the crystal, the excess free energy was about 1000 time less than the typical statistical errors. Since our simulations yield such a small free-energy difference for liquid in contact with the flat wall at $b = 0.0003\sigma$, it is clear that step 6b will yield a similar negligible value and hence this step can effectively be ignored. In general, our simulations indicate a negligible value (less than $10^{-4} k_{\rm B}T/\sigma^2$) for the liquid-flat wall free-energy difference per unit area and hence that of step 6b as well if $b \sim 10^{-4}\sigma$.

We carried out several independent runs for one system size, in both the forward and reverse directions to check the reversibility of step 6b and obtained the free-energy difference from runs that yielded the least hysteresis [27,33]. Our simulation results showed a negligible contribution for this step of the order of $5 \times 10^{-5} k_{\rm B}T/\sigma^2$ for the (100) and (111) orientations and of the order $5 \times 10^{-4} k_{\rm B}T/\sigma^2$ for the (110) orientation. Since the combined statistical and numerical errors in the previous steps (1–6a) are in the range $0.003 k_{\rm B}T/\sigma^2$–$0.005 k_{\rm B}T/\sigma^2$, this last step was not performed for other system sizes at which simulations were carried out. The free-energy difference in the various steps can be computed as

$$\Delta F_i = \int_0^1 \left\langle \frac{\partial H_{\rm i}}{\partial \lambda} \right\rangle d\lambda, \tag{12}$$

where i varies from 1 to 6 corresponding to the six steps. The interfacial free energy $\gamma_{\rm cl}$ is obtained by adding the free-energy differences corresponding to the six steps, divided by the total interfacial area A,

$$\gamma_{\rm cl} = \frac{\sum_{i=1}^{6} \Delta F_{\rm i}}{A}, \tag{13}$$

with $A = 2L_{\rm x}L_{\rm y}$ (the factor 2 takes into account the presence two independent planar crystal-liquid interfaces; cf. Fig. 1).

IV. SIMULATION DETAILS

Molecular dynamics simulations were carried out in the canonical ensemble with the total number of particles $N = N_{\rm l} + N_{\rm c}$, volume V and temperature T maintained constant. Constant temperature was achieved by assigning every 200 time steps random velocities to the particles distributed according to the Maxwell-Boltzmann distribution. Newton's equations of motion were integrated according to the velocity Verlet algorithm [42]. During steps 1–5 of our TI scheme, a time step $\Delta t_{\rm large} = 0.0005\tau$ (with $\tau = \sqrt{m\sigma^2/\epsilon}$) was used. In the sixth step, to take into account the extremely-short-range forces due to the Gaussian flat wall, a multiple-time-step scheme [31] was applied where, in combination with $\Delta t_{\rm large}$, a smaller time step of $\Delta t_{\rm small} = 0.000\,025\tau$ was used. It was observed that this slowed down the simulations by approximately a factor of 2.

The coexistence densities for the inverse-power potential (1), as computed using the free-solidification method [6,43], at the temperature $T = 1.0$, are $\rho_{\rm l}^{\rm inv} = 0.933\sigma^{-3}$ for the liquid phase and $\rho_{\rm c}^{\rm inv} = 1.030\sigma^{-3}$ for the crystal phase [44]; the coexistence pressure is $P_{\rm co}^{\rm inv} = 11.48 k_{\rm B}T/\sigma^3$. In comparison, the coexistence parameters of the actual hard-sphere system are $\rho_{\rm l}^{\rm HS} = 0.940\sigma^{-3}$, $\rho_{\rm c}^{\rm HS} = 1.041\sigma^{-3}$, and $P_{\rm co}^{\rm HS} = 11.576 k_{\rm B}T/\sigma^3$ [6].

From these coexistence values one can define an effective dimensionless diameter $\sigma^{\rm eff} = \sigma(\rho_{\rm c}^{\rm HS}/\rho_{\rm c}^{\rm inv})^{-1/3}$, which can be used as a scaling parameter to compare the two systems. Such an effective diameter can also be obtained using the coexistence pressure value as well as the coexistence density of the

TABLE I. Free-energy differences per unit area $\Delta F/A$ (in units of $k_{\rm B}T/\sigma^2$), corresponding to steps 1–6 for the (100), (110), and (111) orientations of the crystal-liquid interface with the dimensions $20.43 \times 20.43 \times 78.58$, $20.43 \times 20.0 \times 80.02$, and $21.17 \times 20.0 \times 81.66$, respectively (in units of σ^3). The final value of $\gamma_{\rm cl}$ for each orientation is specified in the last line of the table. The quantities within parentheses correspond to the statistical error in the last digit shown. For extremely small numerical values [see data for the (100) and (111) orientations] both the free-energy difference and the error are multiplied by the same power of 10.

Step	(100)	(110)	(111)
1	0.0532(2)	0.0532(2)	0.0532(2)
2	$0.0044(5) \times 10^{-2}$	0.001 93(7)	$0.006(5) \times 10^{-4}$
3	0.993(3)	0.970(4)	0.894(2)
4	0.429(4)	0.409(1)	0.370(1)
5	− 0.880(3)	− 0.841(1)	− 0.763(2)
6	− 0.0035(2)	− 0.020(1)	− 0.0020(1)
$\gamma_{\rm cl}$	0.592(6)	0.573(4)	0.552(3)

liquid. It is observed that using the crystal coexistence density and the coexistence pressure as the scaling variable leads to the same effective diameter, viz., $\sigma^{\rm eff} = 1.0035\sigma$, while use of the liquid coexistence density leads to a slightly lower effective diameter $\sigma^{\rm eff} = 1.0024\sigma$. We will use the effective diameter value $\sigma^{\rm eff} = 1.0035\sigma$ to compare the crystal-liquid interfacial free energy obtained for the inverse power-law model with the hard-sphere values. The equivalent values for the hard-sphere model are obtained as $\gamma_{\rm cl}^{\rm HS} = \gamma_{\rm cl}^{\rm inv}\sigma^{\rm eff^2}/k_{\rm B}T$, where $\gamma_{\rm cl}^{\rm inv}$ is the interfacial free energy corresponding to the inverse power-law potential.

We obtain $\gamma_{\rm cl}$ for the (100), (110), and (111) orientations of the face-centered-cubic crystal with respect to the liquid at the interface. To study finite-size effects, simulations were carried out at various system sizes for the (100) orientation of the interface, ranging from around 7000 to 34 000 particles, with various lateral dimensions and with a total longitudinal dimension of about 80σ. For the other two orientations, simulations were carried out only at the largest system sizes. The dimensions of our system along with the total number of particles are specified in Table I.

To generate initial configurations, liquid and crystal phases were equilibrated for about 2×10^6 time steps (in steps of $\Delta t_{\rm large}$) at their respective coexistence densities. Both phases were simulated in cells of identical dimensions with $N_{\rm l} < N_{\rm c}$ since $\rho_{\rm l} < \rho_{\rm c}$. To calculate $\gamma_{\rm cl}$ via TI, independent runs were carried out at 50–100 values of equally spaced intervals of λ between the initial and final states in order to obtain smooth thermodynamic integrands.

Instead of doing a sequential TI simulation, where the system is first equilibrated at one value of λ and the thermodynamic derivative $\partial U/\partial\lambda$ is computed and then λ is increased to the next higher value and the process is repeated until the final value of λ is reached, here we simultaneously carry out simulations at the various values of λ. At each value of λ, the system was first equilibrated at $\lambda = 0$ for 10^4 time steps and then λ was continuously increased until the desired value of λ was reached. The number of time steps to carry out this switch varied from 2.5×10^5 to 10^6 time steps for the various TI steps. After the desired value λ_i was reached, the system was further equilibrated for times varying from 10^6 to 4×10^6 time steps. Then the production runs were carried out over a period varying from 10^6 to 5×10^6 time steps for the different TI steps to obtain the desired statistical accuracy.

For steps 3–5, a cubic spline interpolation of the bare data was performed to obtain the thermodynamic integrand at 100 intervals between $\lambda = 0$ and 1. Then Simpson's rule was used to numerically calculate the integral. For steps 1, 2, and 6, the thermodynamic integrals were calculated numerically using the trapezoidal rule from the bare data. Statistical errors were calculated by partitioning the production runs into five blocks and then determining the standard deviation from these five samples.

To check the reversibility of each step in the TI scheme, simulations were also carried out in the reverse direction, to detect any hysteresis in the transformation. The initial state for the reverse TI simulations corresponded to the final state of the forward TI path. The final values for $\gamma_{\rm cl}$ reported in Table I correspond to an average of the free-energy differences obtained from the forward and reverse TI simulations.

V. RESULTS

The thermodynamic integrands for the various steps are plotted in Figs. 2–5 for the (100) orientation of the crystal-liquid interface. The data correspond to the largest system size of 32 205 particles with dimensions $20.43 \times 20.43 \times 78.58$ (in units of σ^3). Figure 2 shows the thermodynamic integrand corresponding to steps 1 and 2 of our scheme. It is clear that the area under the thermodynamic integrand curve corresponding to the crystal is negligible as compared to the liquid. Since the crystal is positioned symmetrically with respect to the two ends of the simulation cell, the location of the flat walls (at $z = 0$ and L_z) coincides with a density minimum between two crystalline layers. Moreover, the crystal has a small diffusivity as compared to the liquid. Therefore, the free-energy cost of

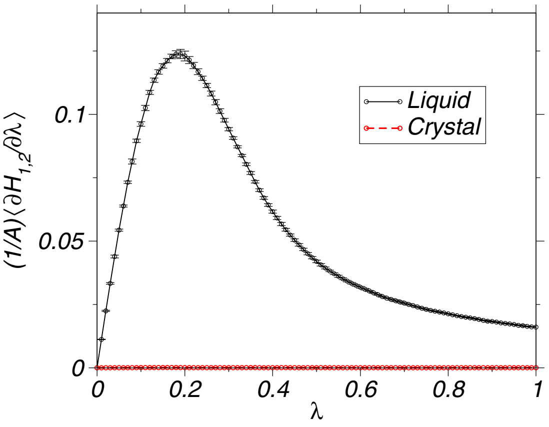

FIG. 2. (Color online) Thermodynamic integrand for steps 1 and 2 for the liquid and crystal phases, respectively, at $T = 1.0$ and the (100) orientation of the crystal. Error bars in this and subsequent figures represent one standard deviation.

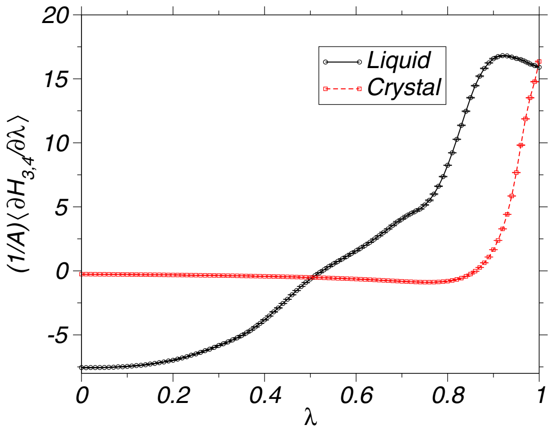

FIG. 3. (Color online) Thermodynamic integrand corresponding to steps 3 and 4, for the liquid and (100) orientation of the crystal, respectively, at the temperature $T = 1.0$.

inserting a flat wall in the crystal is negligible compared to that in the liquid.

For the (100), (110), and (111) orientations of the crystal, $\Delta F_2/A = 4\times10^{-5} \pm 1\times10^{-5}$, $1.8\times10^{-3} \pm 4\times10^{-5}$, and $7.66\times10^{-7} \pm 1.94\times10^{-7}$, while $\Delta F_1/A = 0.053 \pm 2\times10^{-4}$ (in units of k_BT/σ^2). The above data corresponded to $b = 0.027\sigma$. The smoothness of the integrand and the smallness of the error bars in Fig. 2 indicate the lack of hysteresis in our TI scheme. Due to the perfect overlap between the forward and reverse thermodynamic integrands, Fig. 2 shows only the curves corresponding to the forward transformation. For step 1, the difference between the forward and reverse TI results was $2\times10^{-4}k_BT/\sigma^2$ and for the different orientations in step 2, the hysteresis was always less than $4\times10^{-5}k_BT/\sigma^2$.

It is to be noted that unlike in our previous work [35], where an extremely-short-range wall was inserted from the very first step onward, yielding a negligible contribution, here step 1 yields a free-energy difference that cannot be ignored (almost 10% of the final value for $\gamma_{\rm cl}$). This is because the Gaussian flat wall has a slightly longer range (of the same order as the interaction potential itself). The reason for inserting this slightly-longer-range wall, apart from computational efficiency as mentioned previously, has to do with the hysteresis observed in step 3, when the liquid is arranged into an ordered structure near the interface. A relatively-longer-range flat wall induces, at the end of step 1, layering in the liquid near the flat wall, which is compatible with the ordered structure that would be formed near the interface by the structured wall. This results in a smoother thermodynamic integrand. However, in the presence of an extremely-short-range wall (for example, with $b = 3\times10^{-4}\sigma$), the structure near the interface, at the end of step 1, is the same as in the bulk. This leads to hysteresis errors in step 3 and the transformation is not smooth anymore, unless the system is equilibrated for a sufficiently long time.

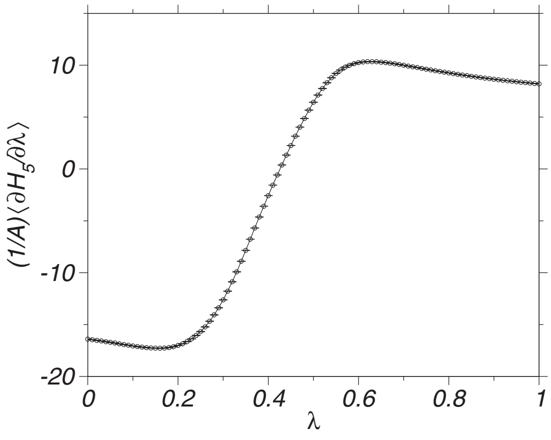

FIG. 4. Thermodynamic integrand for step 5 at $T = 1.0$, bringing the (100) orientation of the crystal in contact with the liquid.

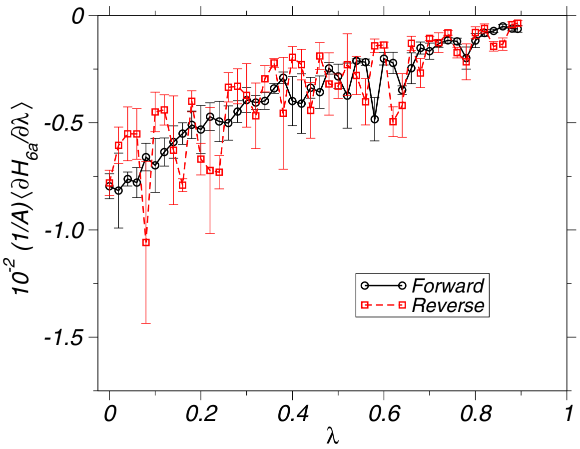

FIG. 5. (Color online) Thermodynamic integrands for the forward and reverse processes corresponding to step 6a, towards reducing the range of the flat wall.

In Fig. 3, thermodynamic integrands corresponding to steps 3 and 4 are shown. We obtained excellent overlap between the forward and reverse thermodynamic integrand curves and therefore only data corresponding to the forward transformation is reported. For step 3, hysteresis between the forward and reverse TI calculations was less than $5\times10^{-3}k_BT/\sigma^2$, while for step 4 the same was less than $1\times10^{-3}k_BT/\sigma^2$ for all three orientations.

At the end of step 3, the liquid is ordered into crystalline layers near the interface. Therefore, the structured wall induces precrystallization of the liquid even at the bulk liquid coexistence density [45]. Since the liquid is already ordered into a structure compatible with the crystal, the next transformation, step 5, corresponding to joining the liquid and crystal phases, occurs smoothly as shown in Fig. 4. The hysteresis between the forward and reverse TI paths was less than $7\times10^{-3}k_BT/\sigma^2$ for the various orientations and system sizes considered in this work.

The final step consists of two substeps. In step 6a, we reduce the range of the Gaussian flat wall to an extremely small value. As specified in Sec. III, the parameter b is changed from 0.027σ [corresponding to a range of 0.1σ, with the range considered to be the distance at which $u_{\rm fw}(z_{iw})$ decays to about $1\times10^{-4}k_BT$] to $3\times10^{-4}\sigma$ (corresponding to a range of about $10^{-3}\sigma$). For this range of the potential, the free-energy difference per unit area of a liquid in contact with this flat wall is $5 \times 10^{-4} k_B T/\sigma^2$ and for the various orientations of the crystal it is less than $2 \times 10^{-5} k_B T/\sigma^2$. Clearly, reducing the range of the flat wall by about 100 times also reduces the free-energy difference by about the same factor.

In step 6a, the range of the potential was modified by varying λ from 0 to 0.894. At $\lambda = 1.0$, the range of the flat wall would be zero. Clearly, to choose an appropriate final value of λ in step 6a, the strategy would be to first compute the accumulated free-energy difference up to step 5. Depending upon the desired accuracy, a value is chosen that is much less than the statistical and numerical errors in the combined steps 1–5. From the ratio of this value and $\Delta F_1/A$, a factor is obtained and multiplying it with the range of the flat-wall potential in step 1, a new range can be calculated, from which the appropriate final value of λ in step 6a can be deduced using Eq. (3). By this strategy, step 6b would become redundant, as argued in Sec. III.

To check whether the resultant flat wall at the end of step 6a produced any artifacts such as a change of the coexistence pressure, we computed the normal component of the pressure along the z direction as a function of the time and compared it to the coexistence pressures of the bulk phases ($P_{\mathrm{co}}^{\mathrm{inv}} = 11.48 k_B T/\sigma^3$). However, as Fig. 6 clearly shows, the coexistence pressure of the crystal-liquid interface in the presence of an extremely-short-range flat wall is in good agreement with the bulk coexistence pressure.

In Fig. 5, we plot the thermodynamic integrands corresponding to the forward and reverse paths of step 6a. Though the curves are a bit noisy compared to the previous steps, the magnitude of the integrands is also very small and hysteresis between the forward and reverse calculations is $5 \times 10^{-4} k_B T/\sigma^2$, with $\Delta F_{6a}/A = -0.0035 \pm 0.0002 k_B T/\sigma^2$. For the (110) and (111) orientations, the contributions from step 6a are -0.020 ± 0.001 and -0.002 ± 0.001 (in units of $k_B T/\sigma^2$).

We have carried out several independent runs corresponding to step 6b and from the runs with the least hysteresis, we extracted the free-energy difference, for one system size. However, for all three orientations the magnitude of the contribution was less than $5 \times 10^{-4} k_B T/\sigma^2$ and hence the thermodynamic integrands are not shown and were not added to the final value of γ_{cl}. The contribution to the total free-energy difference corresponding to the various steps, for the largest system size considered in this work ($20.43\sigma \times 20.43\sigma \times 78.58\sigma$), is shown as a histogram in Fig. 7 for the (100) orientation of the crystal-liquid interface. In addition, Table I shows the free-energy differences accumulated in steps 1–6 for all three orientations of the crystal-liquid interface corresponding to the largest system size.

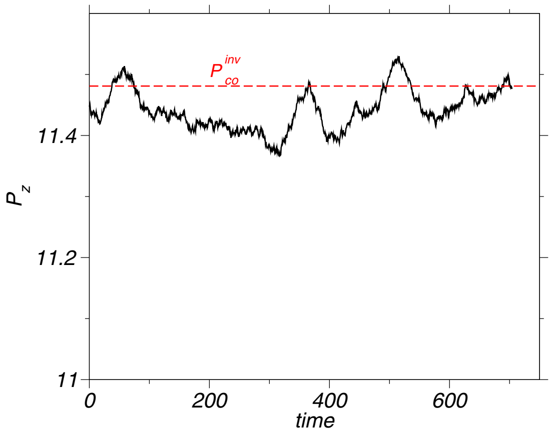

FIG. 6. (Color online) Evolution of the normal component of pressure P_z at the end of step 6a, after equilibrium is reached. The red line denotes the bulk coexistence pressure.

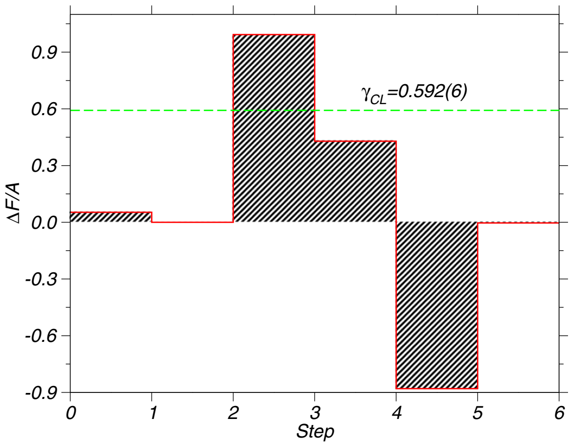

FIG. 7. (Color online) Histogram showing free-energy differences per unit area $\Delta F/A$ corresponding to steps 1–6 (slanted stripes) for the (100) orientation of the crystal-liquid interface with the dimensions $20.43 \times 20.43 \times 78.58$ (in units of σ^3) and the total interfacial free energy γ_{cl} (dashed horizontal line). All free-energy differences per unit area are in units of $k_B T/\sigma^2$.

The final value of γ_{cl} after adding the contributions from each step is reported in Table II for the three orientations and for various system sizes [only for the (100) orientation]. Using the scaling parameter $\sigma^{\mathrm{eff}} = 1.0035\sigma$, the equivalent interfacial free energy for the hard-sphere potential is also specified. Data from the cleaving-wall method corresponding to the pure hard-sphere potential [27] and also for the inverse-power potential extrapolated to the hard-sphere limit ($n \to \infty$) [24] are reported. While our results are slightly higher than those obtained for the former case, they are in good agreement with the latter, within the reported errors. Another TI approach reported recently yielded a similar value for the (100) orientation of the hard-sphere crystal-liquid interface [46].

To study systematic errors arising from finite-size effects we have carried out simulations for the (100) orientation of the crystal-liquid interface at various lateral dimensions ($L_x \times L_y$), keeping the longitudinal dimension fixed at 78.58σ. Recently, Schmitz *et al.* [34] identified the finite-size corrections and proposed a scaling relation to obtain reliable estimates for the interfacial free energies in the thermodynamic limit. According to them, the leading finite-size corrections to the interfacial free energy in the thermodynamic limit are described by the following relation [34,37]:

$$\gamma_{L,L_z} = \gamma_\infty - A\frac{\ln L_z}{L^2} + B\frac{\ln L}{L^2} + \frac{C}{L^2}, \qquad (14)$$

TABLE II. Interfacial free energy $\gamma_{\mathrm{cl}}^{\mathrm{inv}}$ (in units of $k_{\mathrm{B}}T/\sigma^2$) for different system sizes corresponding to various orientations of the crystal-liquid interface. The interfacial free energies for the pure hard-sphere system obtained by using a scaling parameter are also shown (see the text). For comparison, data from the cleaving-wall methods for the pure hard-sphere (HS) system [27] and for the inverse power-law (IP) potential in the hard-sphere limit [24] are also reported. Dimensions $L_x \times L_y \times L_z$ are in units of σ^3. For the (100) orientation of the crystal-liquid interface, the interfacial free energy in the thermodynamic limit is extrapolated from the values of γ_{cl} at the various system sizes using the L^{-2} and $\ln(L)L^{-2}$ scalings (see the text).

Orientation	N	System size	$\gamma_{\mathrm{cl}}^{\mathrm{inv}}$	$\gamma_{\mathrm{cl}}^{\mathrm{HS}}$	Cleaving (HS)	Cleaving (IP)
100	6860	9.43 × 9.43 × 78.58	0.581 ± 0.005	0.585 ± 0.005		
100	9338	11.0 × 11.0 × 78.58	0.584 ± 0.007	0.588 ± 0.007		
100	121 96	12.57 × 12.57 × 78.58	0.586 ± 0.005	0.590 ± 0.005		
100	154 36	14.15 × 14.15 × 78.58	0.584 ± 0.004	0.588 ± 0.004		
100	190 56	15.72 × 15.72 × 78.58	0.591 ± 0.005	0.595 ± 0.005		
100	230 58	17.29 × 17.29 × 78.58	0.592 ± 0.004	0.596 ± 0.004		
100	322 05	20.43 × 20.43 × 78.58	0.592 ± 0.006	0.596 ± 0.006	0.5820 ± 0.0019	0.592 ± 0.007
100	∞	∞	0.595[a],0.597[b]	0.599[a],0.601[b]		
110	321 06	20.43 × 20.0 × 80.02	0.573 ± 0.004	0.577 ± 0.004	0.5590 ± 0.0020	0.571 ± 0.006
111	339 59	21.17 × 20.0 × 81.66	0.552 ± 0.003	0.556 ± 0.003	0.5416 ± 0.0031	0.557 ± 0.007

[a] The L^{-2} scaling.

[b] The $\ln(L)L^{-2}$ scaling.

where A, B, and C are constants and $L = L_x = L_y$ corresponds to the lateral dimension of our system.

The second term in Eq. (14) is identified with the translational entropy of the system arising from the movement of the crystal-liquid interface. Since the flat walls restrict the movement of the crystal-liquid interface, this term can be neglected in our TI scheme. In Fig. 8, we plot γ_{cl} as a function of $1/L^2$ and $\ln(L)/L^2$ separately. Extrapolating the data linearly yields γ_{cl}, the equivalent hard-sphere crystal-liquid interfacial free energy in the thermodynamic limit and for the $1/L^2$ and $\ln(L)/L^2$ scalings, we obtain the values $0.599 k_{\mathrm{B}}T/\sigma^2$ and $0.601 k_{\mathrm{B}}T/\sigma^2$, respectively.

In comparison to the values of γ_{cl} corresponding to the smallest system sizes considered, the thermodynamic limit value is around 3% higher, indicating that finite-size corrections cannot be ignored in order to obtain a reliable estimate. The linear scaling observed in Fig. 8 also indicates that capillary fluctuations are not suppressed on account of the flat walls. It is also to be noted that values of γ_{cl} obtained in the thermodynamic limit for the (100) orientation of the crystal-liquid interface are about 6%–7% less than those corresponding to the capillary fluctuation [28] and tethered Monte Carlo approach [29]. More research is needed to understand the origin of this discrepancy.

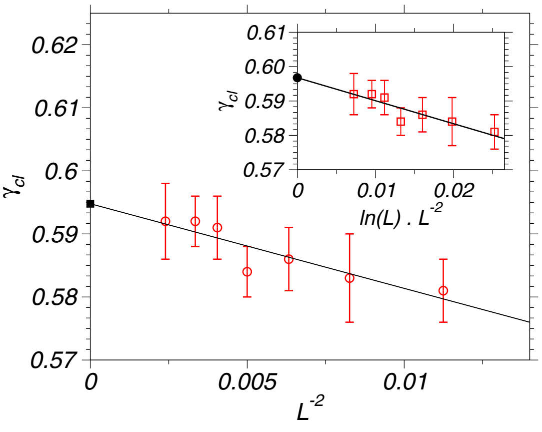

FIG. 8. (Color online) Interfacial free energy γ_{cl} (in units of $k_{\mathrm{B}}T/\sigma^2$) as a function $1/L^2$, where $L = L_x = L_y$, for the (100) orientation of the crystal-liquid interface with the longitudinal dimension $2L_z = 78.58\sigma$. The inset shows γ_{cl} as a function of $\ln(L)/L^2$. Closed symbols correspond to the γ_{cl} values in the thermodynamic limit. The straight lines are a linear fit to the data.

VI. CONCLUSION

We have obtained the crystal-liquid interfacial free energy for the hard-sphere system via a thermodynamic integration scheme. Good agreement of our results with other computational approaches indicates the success of our TI scheme even for short-range interaction potentials. The flat Gaussian walls introduced in this scheme circumvent the problem of achieving a reversible transformation due to the movement of the crystal-liquid interface. These flat walls suppress the movement of this interface and at the same time do not affect the capillary fluctuations. Use of frozen-in crystalline layers to act as structured walls induces ordering in the liquid compatible with the crystal structure and leads to a smooth thermodynamic transformation to the desired final state. The scheme described here could also be used with a Monte Carlo sampling, which in the case of hard spheres would avoid the need for an event-driven code.

Our results also indicate that finite-size errors have to be accounted for in order to obtain accurate estimates for γ_{cl}. The accurate values for the interfacial free energy obtained in this work can be used to validate future density-functional theory approaches, which in the past have yielded higher values as compared to a TI calculation [28]. Furthermore, a TI calculation of γ_{cl} using our scheme is necessary for the pure hard-sphere system to be able to compare with existing values.

ACKNOWLEDGMENT

The authors acknowledge financial support from the German DFG SPP 1296, Grant No. HO 2231/6-3.

[1] B. J. Alder and T. E. Wainright, J. Chem. Phys. **27**, 1208 (1957).
[2] A. Mulero, in *Theory and Simulation of Hard-Sphere Fluids and Related Systems*, edited by A. Mulero, Lecture Notes in Physics Vol. 753 (Springer, Berlin, 2008).
[3] S. Auer and D. Frenkel, Nature (London) **409**, 1020 (2001).
[4] M. Amini and B. B. Laird, Phys. Rev. Lett. **97**, 216102 (2006).
[5] T. Zykova-Timan, R. E. Rozas, J. Horbach, and K. Binder, J. Phys.: Condens. Matter **21**, 464102 (2009).
[6] T. Zykova-Timan, J. Horbach, and K. Binder, J. Chem. Phys. **133**, 014705 (2010).
[7] L. Filion, M. Hermes, R. Ni, and M. Dijkstra, J. Chem Phys. **133**, 244115 (2010).
[8] W. A. Curtin, Phys. Rev. B **39**, 6775 (1989).
[9] D. W. Marr and A. P. Gast, Langmuir **10**, 1348 (1994).
[10] D. W. Marr, J. Chem. Phys. **102**, 8283 (1995).
[11] T. Gruhn and P. A. Monson, Phys. Rev. E **64**, 061703 (2001).
[12] B. O'Malley and I. K. Snook, Phys. Rev. Lett. **90**, 085702 (2003).
[13] E. Zaccarelli, C. Valeriani, E. Sanz, W. C. K. Poon, M. E. Cates, and P. N. Pusey, Phys. Rev. Lett. **103**, 135704 (2009).
[14] T. Kawasaki and H. Tanaka, Proc. Natl. Acad. Sci. USA **107**, 14036 (2010).
[15] T. Schilling, H. J. Schöpe, M. Oettel, G. Opletal, and I. Snook, Phys. Rev. Lett. **105**, 025701 (2010).
[16] A. W. Adamson and A. P. Gast, *Physical Chemistry of Surfaces* (Wiley-Interscience, New York, 1997).
[17] D. Turnbull and R. E. Cech, J. Appl. Phys. **21**, 804 (1950).
[18] D. Turnbull, J. Appl. Phys. **21**, 1022 (1950).
[19] D. Turnbull, J. Chem. Phys. **20**, 411 (1952).
[20] D. Woodruff, *The Solid-Liquid Interface*, 1st ed. (Cambridge University Press, London, 1973).
[21] W. A. Tiller, *The Science of Crystallization: Microscopic Interfacial Phenomena* (Cambridge University Press, New York, 1991).
[22] R. L. Davidchack and B. B. Laird, Phys. Rev. Lett. **85**, 4751 (2000).
[23] A. Cacciuto, S. Auer, and D. Frenkel, J. Chem. Phys. **119**, 7467 (2003).
[24] R. L. Davidchack and B. B. Laird, Phys. Rev. Lett. **94**, 086102 (2005).
[25] B. B. Laird and R. L. Davidchack, J. Phys. Chem. B **109**, 17802 (2005).
[26] R. L. Davidchack, J. R. Morris, and B. B. Laird, J. Chem. Phys. **125**, 094710 (2006).
[27] R. L. Davidchack, J. Chem. Phys. **133**, 234701 (2010).
[28] A. Härtel, M. Oettel, R. E. Rozas, S. U. Egelhaaf, J. Horbach, and H. Löwen, Phys. Rev. Lett. **108**, 226101 (2012).
[29] L. A. Fernandez, V. Martin-Mayor, B. Seoane, and P. Verrocchio, Phys. Rev Lett. **108**, 165701 (2012).
[30] T. P. Straatsma, M. Zacharias, and J. A. MacCammon, *Computer Simulations of Biomolecular Systems* (Escom, Keiden, 1993).
[31] D. Frenkel and B. Smit, *Understanding Molecular Simulation* (Academic, San Diego, 2002).
[32] R. L. Davidchack and B. B. Laird, Phys. Rev. E **54**, R5905 (1996).
[33] R. L. Davidchack and B. B. Laird, J. Chem. Phys. **118**, 7651 (2003).
[34] F. Schmitz, P. Virnau, and K. Binder, Phys. Rev. Lett. **112**, 125701 (2014); Phys. Rev. E **90**, 012128 (2014).
[35] R. Benjamin and J. Horbach, J. Chem. Phys. **141**, 044715 (2014).
[36] D. C. Rapaport, *The Art of Molecular Dynamics Simulation* (Cambridge University Press, Cambridge, 2004).
[37] K. Binder, Phys. Rev. A **25**, 1699 (1982).
[38] E. Lange, J. B. Caballero, A. M. Puertas, and M. Fuchs, J. Chem. Phys. **130**, 174903 (2009).
[39] J. Q. Broughton and G. H. Gilmer, J. Chem. Phys. **84**, 5759 (1986).
[40] R. Benjamin and J. Horbach, J. Chem. Phys. **137**, 044707 (2012); **139**, 039901 (2013).
[41] R. Benjamin and J. Horbach, J. Chem. Phys. **139**, 084705 (2013).
[42] M. P. Allen and D. J. Tildesley, *Computer Simulations of Liquids* (Clarendon, Oxford, 1987).
[43] P. Kuhn and J. Horbach, Phys. Rev. B **87**, 014105 (2013).
[44] R. Rozas, R. Benjamin, and J. Horbach (unpublished).
[45] M. Heni and H. Löwen, J. Phys.: Condens. Matter **13**, 4675 (2001).
[46] J. R. Espinosa, C. Vega, and E. Sanz, J. Chem. Phys. **141**, 134709 (2014).